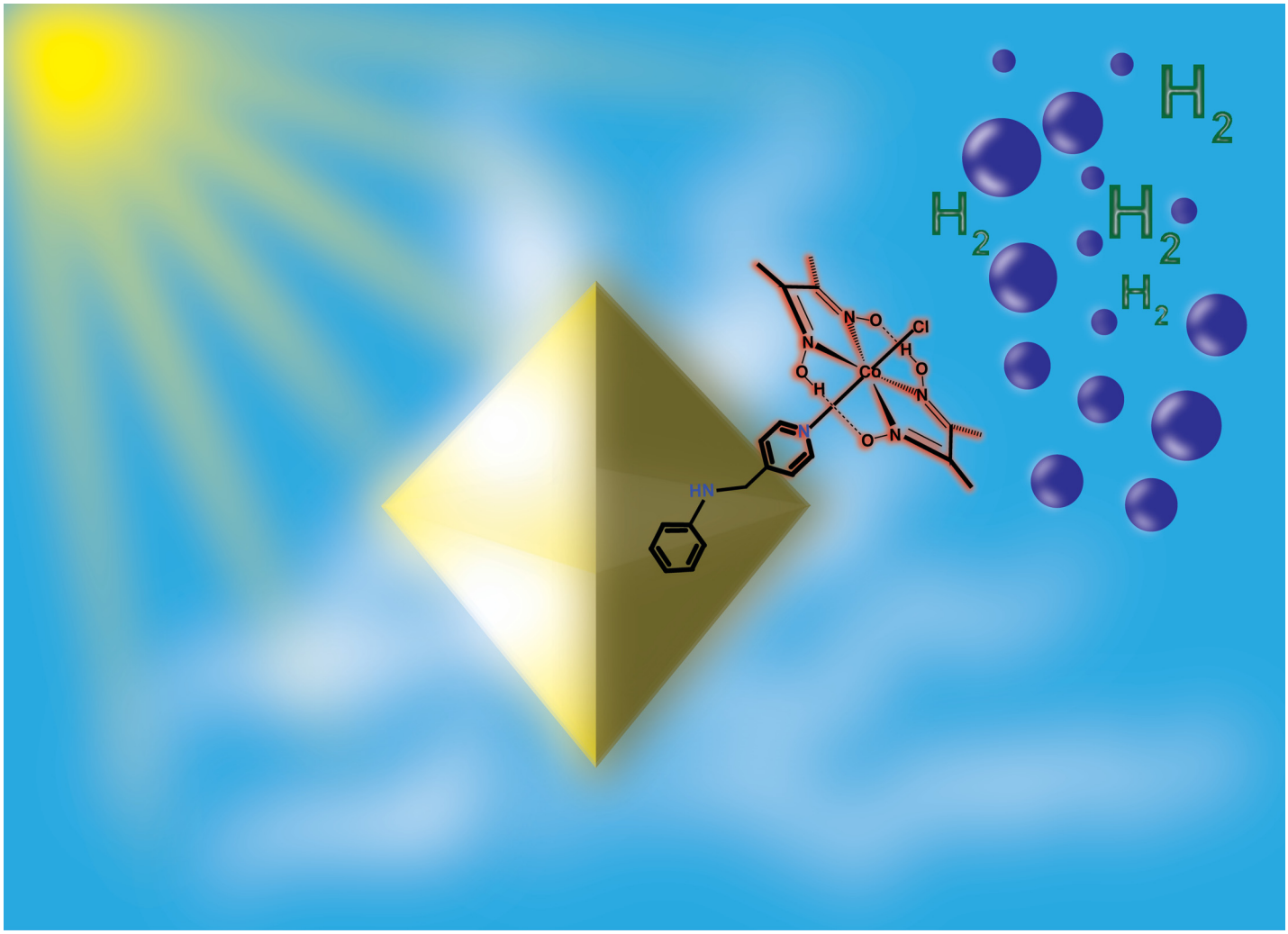

Showcasing research from Professor Dutta's laboratory, Department of Chemistry, Indian Institute of Technology Bombay, Mumbai, India.

Post-synthetic modulation of UiO-66-NH_2 with a cobaloxime catalyst for efficient hydrogen production

A molecular catalyst was strategically embedded on a metal organic framework (MOF). This molecular catalyst-MOF assembly provides a robust template for electrocatalytic and photocatalytic H_2 production in aqueous solution under practical conditions.

As featured in:

See Ujjwal Pal, Arnab Dutta *et al.*, *Energy Adv.*, 2023, **2**, 1116.

ROYAL SOCIETY OF CHEMISTRY

rsc.li/energy-advances

Registered charity number: 207890

Energy Advances

ROYAL SOCIETY OF CHEMISTRY

COMMUNICATION

View Article Online
View Journal | View Issue

Check for updates

Cite this: *Energy Adv.*, 2023, 2, 1116

Received 7th April 2023,
Accepted 19th June 2023

DOI: 10.1039/d3ya00151b

rsc.li/energy-advances

Post-synthetic modulation of UiO-66-NH_2 with a cobaloxime catalyst for efficient hydrogen production†

Saddam Sk, ‡[ab] Sandip Prabhakar Shelake,‡[bc] Dependu Dolui, ‡[d] Suhana Karim,[d] Rajib Ghosh, [e] M. V. Jyothirmai, [f] Annadanam V. Sesha Sainath,[bc] Ujjwal Pal *[ab] and Arnab Dutta *[dg]

Post synthetically-modified UiO-66-NH_2 with a molecular cobaloxime [$Co(DMG)_2Cl_2$] (DMG = dimethylglyoxime) catalyst displays excellent photo-(404 μmol g^{-1} h^{-1}) and electrocatalytic H_2 evolution activity in an aqueous solution. Several analytical and spectroscopic methods, including femtosecond transient absorption spectroscopy and DFT, revealed the unique interaction between cobaloxime and the MOF leading to enhanced catalytic activity.

A hydrogen-based energy economy is considered the mainstay of the futuristic sustainable and carbon-footprint-free energy landscape.[1] In this regard, renewable energy-driven H_2 generation through water-splitting has emerged as one of the top alternatives, where commercially viable technologies for facile and scalable photo and electrocatalytic H_2 evolution reaction (HER) have been probed in detail.[2] A range of competent semiconductor and molecular HER catalysts have been developed in recent years; however, their long-term stability and interaction with the corresponding photosensitizers under catalytic conditions leading to a proficient quantum efficiency remain in doubt.[3] Metal-organic frameworks (MOFs), a class of materials comprised of redox-active metal-cluster nodes connected by an array of organic linkers in all three dimensions, are currently probed as a potential alternative for suitable H_2 production catalysts.[4] UiO-66-NH_2, a unique MOF crafted with Zr-O clusters and NH_2-BDC organic linkers, is widely deployed as a scaffold for hosting molecular catalysts and exploring photo-driven water-splitting reactivity. The organic linker present in the MOF template provides a handle for finetuning the bandgap to the pragmatic visible region from the UV zone.[5] Additionally, the heterojunctions of this MOF allow distinct electrical interactions between the components, leading to novel optoelectronic properties favourable for catalytic HER performance.[4,6] The peripheral functionalities of the organic linker also provide multiple options for their post-synthetic modification and possible inclusion of variable functionality on the MOF architecture.[7–9] Grafting molecular catalysts into MOFs *via* covalent or coordination bonds offers a versatile route for generating novel MOF derivatives while exposing the possibilities of large surface areas and high catalyst loadings.[10]

Cobalt-bis-(dimethylglyoxime) or cobaloxime represents a unique genre of molecular catalyst that displays photo- and electrocatalytic HER activity even in the presence of oxygen.[11] The axial position of the cobaloximes is typically coordinated with N-heterocyclic motifs (pyridine, imidazole, pyrazine), which influences the catalytic response.[12,13] The strategic incorporation of proton-exchanging amino acids on this axial N-heterocycle ensures a rapid proton exchange relay between the bulk solution and cobalt core and significantly improves the catalytic H_2 evolution rate compared to the native cobaloximes. This modification replicates the outer coordination sphere (OCS) effect of the protein scaffold present in metalloenzymes, which is reckoned as one of the major hallmarks that yield the exceptional activity of the enzymes.[14] Such inclusion of the OCS feature has been replicated by native proteins, engineered peptides, amino acids, neurotransmitters, and even drug molecules, where the identical cobaloxime core was deployed as a screening template.[15–20] However, a cobaloxime outlined by a MOF-based OCS has been rarely explored for both photo- and electrocatalytic HER activity.[10]

[a] *Department of Energy & Environmental Engineering, CSIR-Indian Institute of Chemical Technology, Hyderabad, 500007, India. E-mail: upal03@gmail.com, ujjwalpal@iict.res.in*
[b] *Academy of Scientific and Innovative Research (AcSIR), Ghaziabad-201002, India*
[c] *Polymers and Functional Materials and Fluoro-Agrochemicals Department, CSIR-Indian Institute of Chemical Technology, Hyderabad-500007, India*
[d] *Chemistry Department, Indian Institute of Technology Bombay, Powai, Mumbai-400076, India. E-mail: arnab.dutta@iitb.ac.in*
[e] *Radiation & Photochemistry Division, Bhabha Atomic Research Centre, Mumbai-400085, India*
[f] *Department of Chemical Engineering, Indian Institute of Technology Kanpur, Kanpur-208016, India*
[g] *Interdisciplinary Programme in Climate Studies, Indian Institute of Technology Bombay, Powai, Mumbai-400076, India*

† Electronic supplementary information (ESI) available. See DOI: https://doi.org/10.1039/d3ya00151b

‡ These authors have contributed equally.

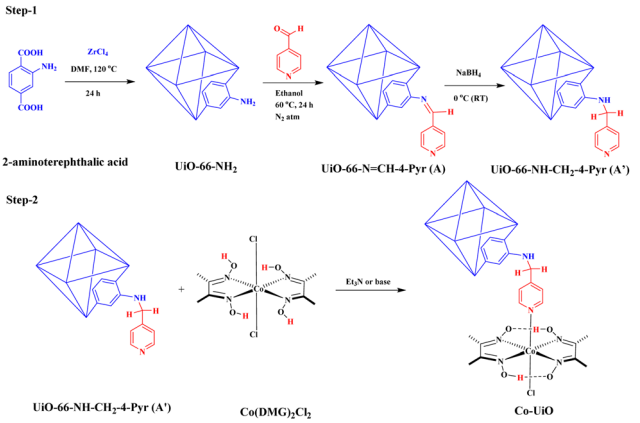

Fig. 1 Synthetic representation for the formation of UiO-66-NH_2 and its post-synthetic modifications with the molecular $Co(DMG)_2Cl_2$ complex.

Herein, a synthetically modified version of UiO-66-NH_2 was appended to an axial pyridine *via* a methylene (–CH_2–) spacer and subsequently linked to a cobaloxime motif (Fig. 1). This new genre of MOF-cobaloxime assembly was further characterized and subsequently investigated for photo and electrocatalytic HER activity. Several complimentary spectroscopic methods were deployed here to unravel the functions of each component in this heterogeneous catalyst. Additionally, femtosecond transient absorbance (fs-TAS) measurements were executed to follow the photoexcited charge transfer between the MOF and cobaloxime, while the fine details of the catalytic performance of the hybrid assembly were unveiled *via* density functional theory (DFT) calculations.

Powdered UiO-66-NH_2 was prepared following the reported procedure.[21] The precursor MOF was reacted with 4-pyridinecarboxaldehyde (4-PC) to generate UiO-66-N = CH-4-Pyr (A) (Fig. 1). Compound A was characterized by NMR spectroscopy as the formation of the imine functionality was supported by the appearance of the signature peak at δ 8.5 ppm and δ 163 ppm in the ^{1}H and ^{13}C NMR spectra, respectively (Fig. S1 and S2, ESI†). This group was then selectively reduced to obtain UiO-66-NH-CH_2-4-Pyr (A′), which was corroborated by the disappearance of the imine signal along with the emergence of secondary amine (Fig. S3, ESI†). Next, A′ was reacted with a $Co(DMG)_2Cl_2$ complex to coordinate it through the appended pyridinyl motif. The appearance of the methyl signified the proper linkage of the cobalt core to the MOF scaffold generating compound Co-UiO (Fig. S4 and S5, ESI†).

The powder XRD data indicate the inherent crystallinity of the UiO-66-NH_2 sample that displayed an octahedral morphology containing a smooth surface and sharp crystal edges (Fig. S6, ESI†). The sequential chemical alterations on the MOF fragment were followed *via* FTIR spectroscopy, where peaks present in the ∼1660–1260 cm^{-1} region showcased the amine to imine transformation (Fig. S7, ESI†).[22] Additionally, the broad signals in the 3300–2800 cm^{-1} zone are assigned to the stretching vibration of –CH_2– motifs. The incorporation of a cobaloxime core was corroborated by the ICP-OES results that indicated a Co : Zr ratio of ∼1.45 in Co-UiO. The quantitative thermogravimetric analysis (TGA) study revealed a subtle difference in the stability of the MOF framework in the presence of the cobalt core. Co-UiO displayed a broad one-step major weight reduction up to ∼550 °C mainly due to the loss of coordinating solvents and thermal decomposition of organic linkers attached to the metal centres, whereas the TGA profile of precursor UiO-66-NH_2 exhibited two decomposition steps at the same temperature window (Fig. S8, ESI†). The comparative N_2 isotherms recorded at 77 K demonstrated porous nature for both UiO-66-NH_2 and Co-UiO (Fig. S9, ESI†). However, the N2 sorption and pore volumes are significantly lower for Co-UiO, which may be attributed to the blocking of the pores by the Co complex and its mass contribution (Table S1, ESI†). Interestingly, the average pore size of Co-UiO (17.74 nm) is ∼5.3 times larger compared to the precursor MOF. Next, X-ray photoelectron spectroscopy (XPS) was deployed to probe the chemical states of the surface elements present in the materials. The existence of Zr, Co, N, C, and O was confirmed during the survey XPS scan (Fig. S10a, ESI†). The Zr emerged as a primary component of the MOF, where it showcased Zr 3d XPS signatures attributable to the Zr^{4+} state generated from Zr–O (181.9 and 184.3 eV) and Zr–Zr bonds (182.7 and 185.1 eV) (Fig. S10b, ESI†). The doublets of the Co 2p signal indicated the presence of both Co^{2+} (780.5 and 796.3 eV) and Co^{3+} (779.6 and 794.6 eV) states in Co-UiO (Fig. S10c, ESI†).[23] The EPR spectrum of Co-UiO supported the presence of a low-spin Co^{2+} centre (Fig. 3a). The XPS results also showcased two N 1s peaks at 398.4 and 399.7 eV corresponding to –NH_2 and –N$=^+$/–NH–$^+$ groups, respectively (Fig. S10d, ESI†).[24,25] In addition, the deconvoluted C 1s XPS region displayed three characteristic peaks related to C–H/C–C (284.2 eV), C–N (285.3 eV), and C–O (287.2 eV) (Fig. S10e, ESI†).[26,27] The existence of C–O (530.4 eV) and Zr–O (531.9 eV) motifs were confirmed from O 1s XPS spectra (Fig. S10f, ESI†).

Next, the MOF-linked heterogenous cobaloxime material was explored for electrocatalytic H_2 production in an aqueous medium. For this study, Co-UiO was immobilized on carbon paper (CP) to develop a tailored working electrode for steady-state linear sweep voltammetry (LSV) studies from slightly acidic (pH ∼ 5.0) to alkaline (pH ∼ 9.0) conditions (Fig. S11–S14, ESI†). The cobaloxime containing Co-UiO exhibited superior HER response compared to the precursor UiO-66-NH_2 at all pH conditions, highlighting the positive impact of incorporating a synthetic catalyst in a strategically modified MOF (Fig. 2a). This electrode-appended Co-UiO demonstrated its best reactivity at pH 9.0, while it leaches out at higher pH conditions during electrocatalysis. The electrocatalytic HER current response typically increases in magnitude compared to the initial CV scans when successive scans are recorded (Fig. S15, ESI†). A chronocoulometric experiment with Co-UiO at pH 9.0 with a fresh carbon paper electrode (CPE) showcased a low current response in the beginning until 2000 s before a steady increase in the reductive current response, replicating the successive CV experiment result (Fig. 2b). This data indicates the possible modification of the electrode material during the experiment. Such a change was not visible for the blank and UiO-66-NH_2-linked electrode beyond 2000 s, which was also noticed in the CV

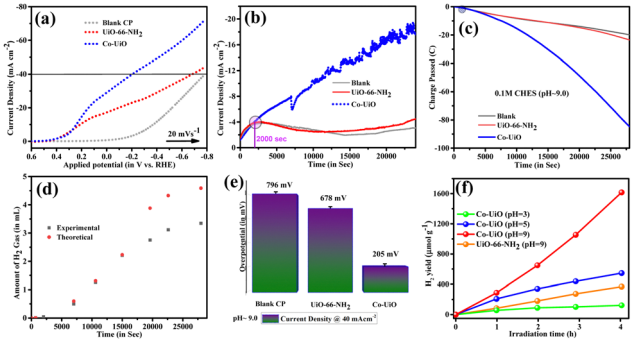

Fig. 2 (a) Comparative linear sweep voltammetry (LSV) data recorded for the catalyst-modified electrodes at pH ~9.0. LSV was recorded after CV stabilised at 20 mV s^{-1} scan rate; data were recorded at room temperature using 0.1 M CHES buffer. The active surface area of the CP-modified electrode was 0.25 cm^2. (b) Chronoamperometric current passed with time during the fixed potential electrolysis at −0.490 V in a 0.1 M CHES buffer (pH ~ 9.0) (the purple circle indicated the boost in HER activity). (c) Chronocoulometric charge passed during the fixed potential electrolysis at −0.472 V (the purple circle indicated the boost in HER activity). [In Figure a, b, c; Gray trace: blank CP, red trace: UiO-66-NH_2 modified CP, and blue trace: Co-UiO modified CP.] (d) The experimentally (black trace) and theoretically (red trace) measured volume of H_2 gas during the bulk electrolysis at pH ~ 9.0. (e) Comparative bar diagram for the overpotential requirement to attain 40 mA cm^{-2} current density during the LSV experiment performed at pH ~ 9.0; and (f) time course of the photocatalytic H_2 production curves.

experiment (Fig. S16, ESI†). This behaviour was also reflected during the charge accumulation, which continued to increase beyond linearity for the Co-UiO sample (Fig. 2c). The formation of H_2 during this experiment was confirmed *via* a gas chromatography (GC) experiment, which showcased excellent faradaic efficiency following an initial lag period (Fig. 2d). Such a difference in the reactivity was attributed to an improved electrochemical specific surface area (ECSA) for Co-UiO compared to UiO-66-NH_2, as recorded from the corresponding specific double layer capacitance (C_{dl}) of the samples (Fig. 2e and Fig. S17, S18, ESI†). Later, we explored the photocatalytic H_2 production by the cobaloxime-anchored MOF in an aqueous solution. Here, a buffer containing dispersed catalyst along with photosensitizer Eosin Y and sacrificial donor TEOA was exposed to photo-irradiation, while the continuous evolution of H_2 was monitored at regular intervals. Co-UiO demonstrated variable photocatalytic HER activity at the pH ~ 3.0 to pH ~ 9.0 region (Fig. 2f and Table S2, ESI†). The maximum H_2 production was noticed at pH ~ 9.0 (~404 μmol H_2 $g_{catalyst}^{-1}$ h^{-1}), which slows down (~70–100 μmol H_2 $g_{catalyst}^{-1}$ h^{-1}) with an increase in solution acidity (pH ~ 3.0–5.0). This drop in reactivity can be attributed to the protonation of the sacrificial electron donor TEOA under acidic conditions. The precursor MOF UiO-66-NH_2 displayed negligible H_2 generation (<25 μmol H_2 $g_{catalyst}^{-1}$ h^{-1}), which highlights the importance of the catalytic cobaloxime core during photocatalysis. Co-UiO represents one of the leading metal catalyst-MOF assemblies, evolving a significant amount of H_2 while superseding even Pt/MOF hybrid photocatalysts (Table S3, ESI†). The powder XRD and SEM analysis of the Co-UiO catalyst were determined after the HER (Fig. S19, ESI†). As revealed by the powder XRD, it (after the HER) shows weak peak intensity but no significant local structural change in the Co-UiO catalyst was observed, which indicates the higher stability of the Co-UiO catalyst. The SEM investigations also confirmed that the morphology of the Co-UiO catalyst was preserved after the HER. This is in agreement with before the HER experiment. This data highlights the long-term stability of the catalyst under experimental conditions. A recyclability test was performed with the same Co-UiO for five continuous 4 hour photocatalytic cycles where ~80% catalytic performance was retained (Fig. S20, ESI†). A series of parallel control experiments illustrated that this photocatalytic HER occurs only in the presence of the active catalyst, photosensitizer, and appropriate photo-irradiation.

The impressive photocatalytic response from Co-UiO led us to explore the possible photoelectron transfer pathways between the MOF and cobaloxime motif in detail. Initially, the UV-Vis diffuse reflectance spectra (DRS) were recorded for precursor cobaloxime, UiO-66-NH_2, and Co-UiO (Fig. S21, ESI†). The pristine UiO-66-NH_2 displayed strong absorption bands in the ~380–450 nm region corresponding to the Zr_6 cluster-based electron transfer (Fig. 3b).[28] The cobaloxime complex exhibited characteristic peaks in the 500–700 nm region, indicating the d–d transitions originating from the Co-core.[29] Both these spectral features are present in Co-UiO, maintaining the properties of cobaloxime and MOF. The influence of cobaloxime binding on the MOF was probed by following the band gap measurement, where Co-UiO showcased a narrower band gap of 2.07 eV compared to the precursor UiO-66-NH_2 (2.93 eV) (Fig. S22, ESI†). Next, the photoluminescence (PL) emission spectrum of Co-UiO was recorded that was substantially weaker than that of pristine UiO-66-NH_2 (Fig. 3c). This data indicates a favourable suppression of radiative recombination of electrons and holes, a key feature for an active photocatalyst. The PL lifetime of the samples was analyzed *via* the time-correlated single-proton counting (TCSPC) method, where a delayed decay was noticed for Co-UiO (13.38 ps) compared to the rapidly decaying pure UiO-66-NH_2 (1.64 ps) (Fig. 3d).

Next, a series of complementary experiments, such as electrochemical impedance spectroscopy (EIS), transient photocurrent

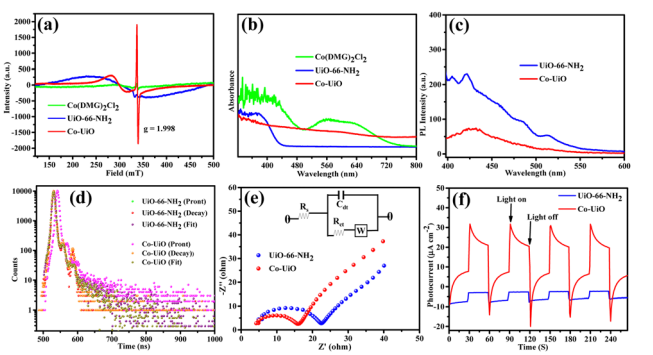

Fig. 3 (a) EPR spectra, (b) UV-Vis diffuse reflectance spectra, (c) photoluminescence (PL) emission spectra, (d) time-resolved photoluminescence decay profile, (e) EIS Nyquist plots (Inset: The equivalent circuit), and (f) transient photocurrent response of the as-synthesised catalyst.

measurement, and Mott Schottky plots, were performed to comprehend the contributory factors behind the enhanced photocatalytic performance by the Co-UiO. Typically, a faster charge transfer rate promotes faster catalysis, which can be detected by a lower electrical resistance in the EIS study.[25,30] As illustrated in Fig. 3e, the inclusion of a cobaloxime core significantly reduced the electrical resistance, highlighted by the lower diameter of the signal for Co-UiO compared to the MOF framework. The strong interfacial chemical linkages in UiO-66-NH_2 possibly ensure a facile electron transfer to the cobaloxime complex to boost photocatalytic water reduction. The photo-driven electron transfer process was further investigated *via* photoelectrocatalytic study, where Co-UiO exhibited better transient photocurrent density ($\sim$30 μA cm^{-2}) than UiO-66-NH_2 (Fig. 3f) under analogous conditions. This data possibly indicates an improved coupling between the molecular Co-complex and MOF scaffold, which increases the separation efficiency of photo-generated electron–hole pairs. The Mott-Schottky analysis was deployed to compute the flat band potentials (E_{fb}) of UiO-66-NH_2 and Co-UiO. The positive slopes for both of these materials indicated their n-type semiconductor nature, while the estimated E_{fb} values for UiO-66-NH_2 and Co-UiO were −0.78 eV and −0.67 eV *vs.* Ag/AgCl, respectively (Fig. S23, ESI†).[31] The positively shifted value for Co-UiO suggests better charge accumulation on the material, which is beneficial for photoinduced electron transport.[32] Typically, the conduction band minimum (CBM) of an n-type semiconductor lies 0.1 V lower than the flat-band potential.[25] Hence, the current values suggest that the CBM for UiO-66-NH_2 and Co-UiO is conducive to H_2 production as it is cathodically positioned compared to the H^+/H_2 potential. According to the bandgap potential as mentioned above, the valence band maximum (VBM) values of UiO-66-NH_2 and Co-UiO were about 2.25 eV and 1.50 eV, respectively.

To discern the influence of cobaloxime functionalization on charge-carrier dynamics of UiO-66-NH_2, ultrafast transient absorbance spectroscopy experiments were performed. The initial experiment with dispersed UiO-66-NH_2 demonstrated a transient absorption signal peaking at 670 nm, and a weak stimulated emission signal at 460 nm (Fig. 4a). The emerging 670 nm signal can be assigned to metal charge transfer from NH_2-BDC to the Zr metal centre. This charge transfers excited state decays rapidly with a lifetime of $\sim$45 ps along with a minor long-lived component (>1 ns) due to the charge-separated state.[33] Interestingly, the covalent functionalization with cobaloxime (Co-UiO) expedites the transient absorption signature (lifetime 10 ps) (Fig. 4b). Comparison of the transient decay signal of UiO-66-NH_2 and its cobaloxime functionalized variant (Co-UiO) demonstrated a remarkably faster decay of the MOF-localized charge transfer state (Fig. 4c). This can be explained invoking fast electron transfer to the cobalt centre leading to the formation of Co(I) species.[34] The ultrafast decay of the MOF-centred excited absorption feature captures the rapid and efficient photoinduced electron transfer to cobaloxime, which subsequently promotes improved H_2 production. Extending this photocatalytic analysis, a plausible charge transfer process from the photosensitizer Eosin Y to Co-UiO catalyst can be hypothesized

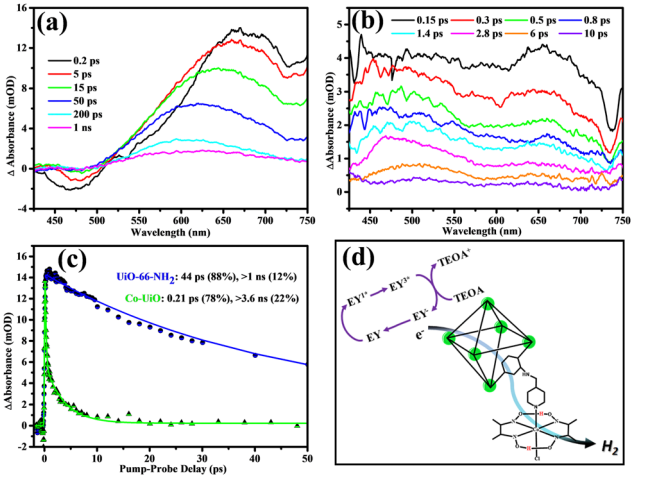

Fig. 4 Ultrafast transient absorption spectral studies of (a) UiO-66-NH_2 and (b) molecular cobaloxime functionalized Co-UiO samples dispersed in the aqueous medium. (c) Comparison of decay kinetics of the two samples at 670 nm. (d) Schematic illustration of the charge transfer path of the Co-UiO catalyst.

(Fig. 4d). After light absorption, EY converts to a singlet excited state $EY^{1}*$ and further generates a triplet excited states $EY^{3}*$ *via* intersystem crossing (ISC).[35] In the presence of sacrificial electron donor TEOA, $EY^{3}*$ is reductively quenched to produce $EY^{-\bullet}$ and $TEOA^+$. Next, strong reducing agent $EY^{-\bullet}$ transfers electrons to the Zr-oxo clusters or the CB of UiO-66-NH_2 to trigger H_2 evolution. Additionally, UiO-66-NH_2 can also be directly excited to generate electrons. The photoexcited electrons on the UiO surface are transferred to the molecular cobaloxime complex, where the protons are reduced to form H_2.

The UiO-66 is constructed with hexa-nuclear Zr_6-octahedron clusters, forming $Zr_6O_4(OH)_4$ nodes through 12 BDC linkers per node. Here, the periodic unit cells of UiO-66 are utilized to construct a neutral cluster model of UiO-66-NH_2 while the dangling bonds of the selected subset were capped with hydrogen atoms resulting in a fully relaxed structure (Fig. S24a and b, ESI†). DFT analysis was performed to calculate the electrostatic potentials along with the frontier molecular orbitals to gain deep insight into the catalytic activity of UiO-66-NH_2. In the catalytic process, the absorption spectrum is a key property to comprehend the mechanism of excited state behaviour under photo-irradiation. Typically, the transition from the highest occupied linker orbital (HOLO) to the lowest unoccupied linker orbital (LULO) is assumed as the absorption threshold, and the corresponding energy required to excite the linker (E_{ads}) is given by: $E_{ads} = E_{LULO} - E_{HOLO}$, where E_{HOLO} and E_{LULO} correspond to the orbital energies. The E_{ads} should be in the visible region to ensure proper utilization of solar light. In addition, the photo-generated electrons should be easily transferred from the photo-excited linker orbital (LULO) to the node's unoccupied d orbitals (LUNO), and the energy required for the ligand-to-metal charge transfer process (E_{LMCT}) is defined as $E_{LMCT} = E_{LUNO} - E_{LULO}$, where E_{LUNO} indicates the energy of the lowest unoccupied node orbital.[36,37] An ideal catalyst should have a negative or close to zero E_{LMCT}

value to prolong the lifetime of the excited states. As displayed in Fig. S24c and d (ESI†), the density of states calculation revealed that both the LULO and HOLO of UiO-66 are dominated by the linker contribution. The high E_{ads} value of UiO-66 (3.51 eV) indicates poor absorption of visible light. In addition, the LULO is located 1.81 eV below the lowest unoccupied metal orbital, suggesting the existence of a positive and large LMCT band. This signifies a shorter lifetime of excited states due to the thermodynamically unfavourable transfer of photogenerated electrons from linker to LUNO, which corroborated the limited catalytic activity observed for the pristine MOF during experiments. The functionalization of the pristine UiO-66 with the NH_2 linker generates new states within the HOLO–LULO gap and moves the HOLO towards LULO to reduce the E_{ads} gap to 2.89 eV. The E_{LMCT} is also decreased after NH_2 functionalization, leading to the stabilization of excited states resulting in enhanced catalytic activity. Therefore, the improved catalytic performance can be attributed to the difference in energy levels, which indicates that rational functionalization of the MOF framework with electron-donating NH_2 groups can be an efficient strategy to modulate their reactivity.

In summary, we have developed a strategy for using the UiO-66-NH_2 framework as a support for anchoring a molecular cobaloxime catalyst. The hybrid Co-UiO catalyst demonstrated encouraging photo and electro-catalytic H_2 activities with excellent stability in an aqueous solution. Future advancements, such as stronger covalent bonding of cobaloxime catalysts with a post-synthetically modified MOF, can generate efficient and robust H_2 production assemblies.

Conflicts of interest

There are no conflicts to declare.

Acknowledgements

This work was supported by the DST HFC research grants (project No: DST/TMD/HFC/2K18/60/(C)/3) Government of India's financial support. S. Sk and S. P. S. thank AcSIR for PhD enrolment. The authors are also grateful to CSIR-IICT (IICT/Pubs./2023/118) for support. A. D. would like to acknowledge support by the Department of Science and Technology, Science and Engineering Research Board (DST-SERB), India for the core research grant (CRG/2020/001239). M. V. J. would like to thank the HPC centre, IIT Kanpur for providing the computational facilities.

Notes and references

1 N. S. Lewis and D. G. Nocera, *Proc. Natl. Acad. Sci.*, 2006, **103**, 15729–15735.
2 P. Ganguly, M. Harb, Z. Cao, L. Cavallo, A. Breen, S. Dervin, D. D. Dionysiou and S. C. Pillai, *ACS Energy Lett.*, 2019, **4**, 1687–1709.
3 M. R. Gholipour, C.-T. Dinh, F. Béland and T.-O. Do, *Nanoscale*, 2015, **7**, 8187–8208.
4 S. Tasleem, M. Tahir and W. A. Khalifa, *Int. J. Hydrogen Energy*, 2021, **46**, 14148–14189.
5 X. Kong, Q. Pan, S. Song, Z. He, T. Zeng and Y. Yu, *J. Phys. Chem. C*, 2021, **125**, 20320–20330.
6 J. Yan, X. Zhang, W. Zheng and L. Y. S. Lee, *ACS Appl. Mater. Interfaces*, 2021, **13**, 24723–24733.
7 J. Canivet, S. Aguado, C. Daniel and D. Farrusseng, *ChemCatChem*, 2011, **3**, 675–678.
8 S. J. Garibay and S. M. Cohen, *Chem. Commun.*, 2010, **46**, 7700–7702.
9 L. Garzón-Tovar, S. Rodríguez-Hermida, I. Imaz and D. Maspoch, *J. Am. Chem. Soc.*, 2017, **139**, 897–903.
10 S. Roy, Z. Huang, A. Bhunia, A. Castner, A. K. Gupta, X. Zou and S. Ott, *J. Am. Chem. Soc.*, 2019, **141**, 15942–15950.
11 D. W. Wakerley, M. A. Gross and E. Reisner, *Chem. Commun.*, 2014, **50**, 15995–15998.
12 D. Dolui, S. Ghorai and A. Dutta, *Coord. Chem. Rev.*, 2020, **416**, 213335.
13 D. Dolui, S. Khandelwal, P. Majumder and A. Dutta, *Chem. Commun.*, 2020, **56**, 8166–8181.
14 B. Ginovska-Pangovska, A. Dutta, M. L. Reback, J. C. Linehan and W. J. Shaw, *Acc. Chem. Res.*, 2014, **47**, 2621–2630.
15 M. Bacchi, G. Berggren, J. Niklas, E. Veinberg, M. W. Mara, M. L. Shelby, O. G. Poluektov, L. X. Chen, D. M. Tiede, C. Cavazza, M. J. Field, M. Fontecave and V. Artero, Cobaloxime-Based Artificial Hydrogenases, (accessed March 11, 2023), https://pubs.acs.org/doi/pdf/10.1021/ic501014c.
16 M. Bacchi, E. Veinberg, M. J. Field, J. Niklas, T. Matsui, D. M. Tiede, O. G. Poluektov, M. Ikeda-Saito, M. Fontecave and V. Artero, *ChemPlusChem*, 2016, **81**, 1083–1089.
17 D. Dolui, S. Khandelwal, A. Shaik, D. Gaat, V. Thiruvenkatam and A. Dutta, *ACS Catal.*, 2019, **9**, 10115–10125.
18 S. Ghorai, S. Khandelwal, S. Das, S. Rai, S. Guria, P. Majumder and A. Dutta, *Dalton Trans.*, 2023, **52**, 1518–1523.
19 A. Q. Mir, S. Saha, S. Mitra, S. Guria, P. Majumder, D. Dolui and A. Dutta, *Sustainable Energy Fuels*, 2022, **6**, 4160–4168.
20 G. Afshan, S. Ghorai, S. Rai, A. Pandey, P. Majumder, G. N. Patwari and A. Dutta, *Chem. – Eur. J.*, 2023, e202203730.
21 J. H. Cavka, S. Jakobsen, U. Olsbye, N. Guillou, C. Lamberti, S. Bordiga and K. P. Lillerud, *J. Am. Chem. Soc.*, 2008, **130**, 13850–13851.
22 J. Zhu, L. Wu, Z. Bu, S. Jie and B.-G. Li, *ACS Omega*, 2019, **4**, 3188–3197.
23 Q. Pan, F. Zheng, D. Deng, B. Chen and Y. Wang, *ACS Appl. Mater. Interfaces*, 2021, **13**, 56692–56703.
24 J. Xu, S. He, H. Zhang, J. Huang, H. Lin, X. Wang and J. Long, *J. Mater. Chem. A*, 2015, **3**, 24261–24271.
25 S. Sk, I. Mondal, A. Mahata, B. M. Abraham, C. Nayak, D. Bhattacharyya, S. N. Jha, R. Ghosh and U. Pal, *ACS Appl. Energy Mater.*, 2022, **5**, 12324–12335.
26 F. Meng, Y. Qin, J. Lu, X. Lin, M. Meng, G. Sun and Y. Yan, *J. Colloid Interface Sci.*, 2021, **584**, 464–473.
27 M. Zhang, Z. Luo, M. Zhou, G. Zhang, K. A. Alamry, L. A. Taib, A. M. Asiri and X. Wang, *Appl. Catal., B*, 2017, **210**, 454–461.
28 Q. Ran, Z. Yu, R. Jiang, L. Qian, Y. Hou, F. Yang, F. Li, M. Li, Q. Sun and H. Zhang, *Catal. Sci. Technol.*, 2020, **10**, 2531–2539.

29 Z. Li, J.-D. Xiao and H.-L. Jiang, *ACS Catal.*, 2016, **6**, 5359–5365.
30 S. Sk, A. Tiwari, B. M. Abraham, N. Manwar, V. Perupogu and U. Pal, *Int. J. Hydrogen Energy*, 2021, **46**, 27394–27408.
31 S. Sk, C. S. Vennapoosa, A. Tiwari, B. M. Abraham, M. Ahmadipour and U. Pal, *Int. J. Hydrogen Energy*, 2022, **47**, 33955–33965.
32 L. Hao, R. Shen, C. Huang, Z. Liang, N. Li, P. Zhang, X. Li, C. Qin and X. Li, *Appl. Catal., B*, 2023, **330**, 122581.
33 T. Goswami, H. Bhatt, D. K. Yadav and H. N. Ghosh, *Phys. Chem. Chem. Phys.*, 2022, **24**, 19121–19143.
34 S. E. Canton, X. Zhang, J. Zhang, T. B. van Driel, K. S. Kjaer, K. Haldrup, P. Chabera, T. Harlang, K. Suarez-Alcantara, Y. Liu, J. Pérez, A. Bordage, M. Pápai, G. Vankó, G. Jennings, C. A. Kurtz, M. Rovezzi, P. Glatzel, G. Smolentsev, J. Uhlig, A. O. Dohn, M. Christensen, A. Galler, W. Gawelda, C. Bressler, H. T. Lemke, K. B. Møller, M. M. Nielsen, R. Lomoth, K. Wärnmark and V. Sundström, *J. Phys. Chem. Lett.*, 2013, **4**, 1972–1976.
35 K. Wang, S. Liu, P. Zhu, M. Yang and Z. Jin, *Energy Fuels*, 2022, **36**, 2058–2067.
36 I. Mondal, A. Mahata, H. Kim, U. Pal, F. D. Angelis and J. Y. Park, *Nanoscale*, 2020, **12**, 17769–17779.
37 I. Mondal, H. Lee, H. Kim and J. Y. Park, *Adv. Funct. Mater.*, 2020, **30**, 1908239.